AMERICAN ACADEMY OF OPHTHALMOLOGY®

Label-Free Imaging of Inflammation at the Level of Single Cells in the Living Human Eye

Yuhua Rui, MD,[1,2] Min Zhang, PhD,[1] Daniel M.W. Lee,[3] Valerie C. Snyder,[1] Rashmi Raghuraman,[1] Elena Gofas-Salas, PhD,[4,5] Pedro Mecê, PhD,[6] Sanya Yadav,[7] Pavan Tiruveedhula, MS,[8] Kate Grieve, PhD,[4,5] José-Alain Sahel, MD,[1] Marie-Hélène Errera, MD,[1] Ethan A. Rossi, PhD[1,3,9]

Purpose: Putative microglia were recently detected using adaptive optics ophthalmoscopy in healthy eyes. Here we evaluate the use of nonconfocal adaptive optics scanning light ophthalmoscopy (AOSLO) for quantifying the morphology and motility of presumed microglia and other immune cells in eyes with retinal inflammation from uveitis and healthy eyes.

Design: Observational exploratory study.

Participants: Twelve participants were imaged, including 8 healthy participants and 4 posterior uveitis patients recruited from the clinic of 1 of the authors (M.H.E.).

Methods: The Pittsburgh AOSLO imaging system was used with a custom-designed 7-fiber optical fiber bundle for simultaneous confocal and nonconfocal multioffset detection. The inner retina was imaged at several locations at multiple timepoints in healthy participants and uveitis patients to generate time-lapse images.

Main Outcome Measures: Microglia and macrophages were manually segmented from nonconfocal AOSLO images, and their morphological characteristics quantified (including soma size, diameter, and circularity). Cell soma motion was quantified across time for periods of up to 30 minutes and their speeds were calculated by measuring their displacement over time.

Results: A spectrum of cell morphologies was detected in healthy eyes from circular amoeboid cells to elongated cells with visible processes, resembling activated and ramified microglia, respectively. Average soma diameter was 16.1 $\pm$ 0.9 μm. Cell movement was slow in healthy eyes (0.02 μm/sec on average), but macrophage-like cells moved rapidly in some uveitis patients (up to 3 μm/sec). In an eye with infectious uveitis, many macrophage-like cells were detected; during treatment their quantity and motility decreased as vision improved.

Conclusions: In vivo adaptive optics ophthalmoscopy offers promise as a potentially powerful tool for detecting and monitoring inflammation and response to treatment at a cellular level in the living eye.

Financial Disclosure(s): Proprietary or commercial disclosure may be found in the Footnotes and Disclosures at the end of this article. *Ophthalmology Science 2024;4:100475*

Supplemental material available at www.ophthalmologyscience.org.

Retinal microglia are the primary resident immune cells[1,2] of the retina. In development, microglia actively prune and sculpt retinal cells and their circuitry.[3] In mature retina, microglia are necessary for healthy visual functioning, through the maintenance of the synapses in the plexiform layers.[4] In the healthy adult retina, microglia exist in a regularly ordered ramified state.[3] In primates, their highest densities are observed in the inner and outer plexiform layers while a small proportion reside in the ganglion cell layer and on the retinal surface.[5] In mice, retinal surface macrophages predominantly include microglia but also include perivascular macrophages and hyalocytes.[6,7] Ramified microglia have cell morphologies that are dendritic in appearance with many processes extending from the soma that constantly survey the local microenvironment.[8] Resting microglia form a network of potential immunoeffector cells[9] that can become activated during inflammation. Depending on the inflammatory stimuli, these cells can exhibit a wide range of actions and roles such as driving acute inflammatory responses and both initiating and regulating lymphocyte-driven adaptive responses.[10,11] Microglia can trigger inflammatory responses to pathogens and tissue trauma and pave the way for the progressive recruitment of circulating myeloid cells such as neutrophils, inflammatory monocytes/macrophages, and lymphocytes into the eye.[11,12]

Though previously inaccessible to direct cellular-level ophthalmic in vivo imaging, recent advances in adaptive

https://doi.org/10.1016/j.xops.2024.100475
ISSN 2666-9145/24

Table 1. Demographic Characteristics of Participants

Category	Participants (n)	Sex		Eye Imaged		Age (yrs), Mean (SD)	Axial Length (mm), Mean (SD)
		Male	*Female*	*OD*	*OS*		
Healthy participant (P)	8	5	3	7	1	30 (6)	24.36 (0.54)
Posterior uveitis patient (Pt)	4	1	3	3	1	51 (13)	23.88 (0.83)

OD = right eye; OS = left eye; SD = standard deviation.

optics ophthalmoscopy have begun to reveal microglial cells and their dynamic activity with high resolution in normal healthy eyes.[8,13,14] Adaptive optics permits high-resolution imaging of the human retina in vivo at a cellular level by compensating for the optical aberrations of the eye.[15] The addition of adaptive optics to multiple ophthalmic imaging modalities, such as adaptive optics scanning light ophthalmoscopy (AOSLO),[16] adaptive optics OCT,[17] and flood illumination adaptive optics[18] have enabled visualization of many of the cell classes within the living human eye, with some retinal cell classes (e.g., cone photoreceptors and retinal pigmented epithelial cells) now accessible in multiple modalities. Over the past several years, the list of retinal cell classes accessible to in vivo

Table 2. Case Description of Uveitis Patients

Patient No. (Pt)	Sex	Age, yrs	Eye	Major Dignosis	Uveitis Duration*	AOSLO Sessions	Treatment	Clinical Features	FFA
1	Male	52	OS	ASPPC	6 d	3 sessions at 0, 26, and 41 days	#1: benzathine G penicillin 24,000,000 units IM once weekly for 2 consecutive weeks)	Irregular, nodular thickening of the retinal pigment epithelium on OCT	N/A
2	Female	69	OD	bilateral PU and retinal vasculitis (periphlebitis)	3 mo	1	4 weeks of PO prednisone (dose was 0.25 mg/kg/d, slow tapering from initial 0.5 mg/kg/d)	resolved periphlebitis OD>OS and resolved papillitis OU	• initial FFA showed leakage from optic disc and retinal vessels. • FFA 3 months later (same day as AOSLO) showed retinal vasculitis less active with reduced leakage noted from retinal vessels OU
3	Female	35	OD	bilateral chronic PU and CSME	8 yrs	2	#1: DEX intravitreal implant 15 months ago; SC ADA restarted 3 weeks ago.† #2: infliximab IV (2 mg/kg) started 3 months prior.‡	peripheral retinal ischemia, no vessel sheathing	FFA acquired 18 and 12 months ago both showed unchanged mid periphery vessels leakage, diffuse capillary staining
4	Female	48	OD	chronic PU and CSME	22 mo	1	IVT for uveitis related CSME (×1), PSTA (×1), DEX implant (×3), FAc IV (×1).	peripheral retinal ischemia, no vessel sheathing	widespread choriocapillaris fluorescein staining, peripapillary vessels leakage nasally

ADA = adalimumab; AOSLO = adaptive optics scanning light ophthalmoscopy; ASPPC = acute syphilitic posterior placoid chorioretinitis; CSME = cystoid macular edema; DEX = dexamethasone intravitreal implant 0.7mg; FAc = fluocinolone acetonide intravitreal implant 0.18 mg; FFA = fundus fluorescein angiography; IM = intramuscular; IV = intravitreal; IVT = triamcinolone acetate intravitreal injections; N/A = not available; OD = right eye; OS = left eye; OU = bilateral; PO = per os; PSTA = posterior subtenon injection of triamcinolone acetonide; Pt = patient; PU = posterior uveitis; SC = subcutaneous.
*Duration of uveitis is counted on initial AOSLO imaging.
†ADA was discontinued for 9 months due to pregnancy.
‡Switching to IV infliximab because ADA did not prevent the occurrence of eye inflammation 2 months after being restarted.

imaging has continued to grow. In adaptive optics OCT, advances toward imaging of additional cell classes, such as retinal ganglion cells and macrophages, have come from higher speed devices with improved image processing and registration that enable the averaging of many volumetric data sets.[8,19,20] In AOSLO, additional cell classes and structures have recently become accessible mostly due to changes in how the light is detected.

Nonconfocal AOSLO has enabled imaging of structures that are not visible using traditional confocal imaging. Unlike confocal imaging where a pinhole aperture is set on the optical axis at the retinal conjugate focal plane to reject light from out of focus retinal layers, the principle behind nonconfocal imaging modes is to purposely acquire the nonconfocal portion of the light distribution that falls outside the confocal aperture detection area. It is thought that these techniques preferentially collect light that has been multiply scattered[21,22] by the retina. The first and simplest approach used in AOSLO consisted of a single aperture displaced from the optical axis.[21,22] This "offset aperture" method was shown to enhance the contrast of certain retinal structures, such as capillary walls.[21] Since then, additional nonconfocal AOSLO setups have been devised that differ in detection pattern and the number of detectors used. Scoles et al[23] showed that splitting the nonconfocal light into 2 portions and directing each to separate detectors yields 2 images of the same area that can be combined to increase image contrast. This "split-detection" setup allowed for the first in vivo imaging of cone inner segments. Later work showed the nonconfocal light distribution could be further subdivided and similarly combined using an offset aperture sequentially positioned at multiple points across the retinal conjugate focal plane. This "multioffset" detection was shown to improve the contrast of retinal ganglion cells[13,24] and presumed microglia.[13] Recently, an additional orthogonal split was added to achieve 4-quadrant detection;[25] this setup, combined with an emboss filtering approach, was shown to reveal the vitreous cortex hyalocytes, and the dynamics of their processes with high contrast. However, this technique was not used for quantification of microglial cell morphology, as the image filtering approach prevented accurate morphological measurements from being obtained.[14] An optical model has been proposed that suggests that all these nonconfocal methods enhance contrast by exploiting spatial variations in the refractive index, in a similar way to phase contrast microscopy.[26,27]

We recently showed that multioffset detection could be improved through the use of a radial detection pattern[13] and spatial frequency-based image fusion.[27] However, sequential multioffset remained inherently slow due to the need to physically move the aperture across the retinal conjugate focal plane for acquisition, resulting in several minutes of acquisition at each retinal location. A further limitation is that the adaptive optics correction and optical quality fluctuates over time as eye movements continuously shift the field of view, reducing the common area of overlap for image fusion. Here we implemented simultaneous multioffset detection using an optical fiber bundle (FB), similar to Mozaffari et al,[28] but in a simplified optical setup using a custom-designed FB based on our recently published optimized radial detection pattern.[13] We evaluated the use of this improved multioffset detection configuration for the quantification of microglia and macrophage-like cell morphology and motility across short timescales in healthy eyes and in patients with inflammation from posterior uveitis.

Methods

Study Approval

This study was approved by the Institutional Review Board of the University of Pittsburgh and adhered to the tenets of the Declaration of Helsinki. Written informed consent was acquired before enrollment for each participant following a detailed explanation of experimental procedures both verbally and in writing. Written informed consent included potential use of participants' deidentified ophthalmology examination results.

Participants

Twelve participants were enrolled; demographic information is shown in Table 1. Eight healthy participants had no known retinal and/or ocular diseases (hereafter referred to as P1−P8). Four patients were recruited from the uveitis clinic of 1 of the authors (M.H.E.). Medical history and treatment information (hereafter referred as Pt1−Pt4) are summarized in Table 2. Before imaging, 1 drop of 1% tropicamide and 1 drop of 2.5% phenylephrine hydrochloride were applied for pupil dilation.

Fiber Bundle-Based Nonconfocal Multioffset AOSLO Imaging

The study was carried out on the Pittsburgh AOSLO (Fig S1, available at www.ophthalmologyscience.org) with the light detection pathway and data acquisition system modified for FB detection as described in detail in Appendix S1 (available at www.ophthalmologyscience.org). Adaptive optics scanning light ophthalmoscopy focus was set to be at the level of the retinal ganglion cell layer for all participants except for Pt1. In Pt1 we imaged the inner retina near the fovea and set the focus to the best plane to visualize the macrophage-like structures that were visible in the raw data. Microglia and macrophage-like cells were manually segmented to quantify morphometry. Independent labeling of microglia and macrophage-like cells was done for static images (3 graders) and for every frame of the time-lapse video clips (2 graders). Detailed descriptions of the image processing and analysis procedures can be found in Appendix S1.

Results

Imaging of Microglia in Healthy Eyes

Only modest differences in nonconfocal image quality were observed when comparing FB detection to our previous sequential multioffset approach, with FB images in general showing slightly improved image quality (Fig S2, available at www.ophthalmologyscience.org). Compared with sequential detection (3−4 minutes per acquisition), the reduced acquisition time for FB detection permitted multiple locations to be imaged and montaged, allowing for microglia to be segmented and quantified across larger retina areas (Fig 3; Fig S4A, available at www.ophthalmologyscience.org).

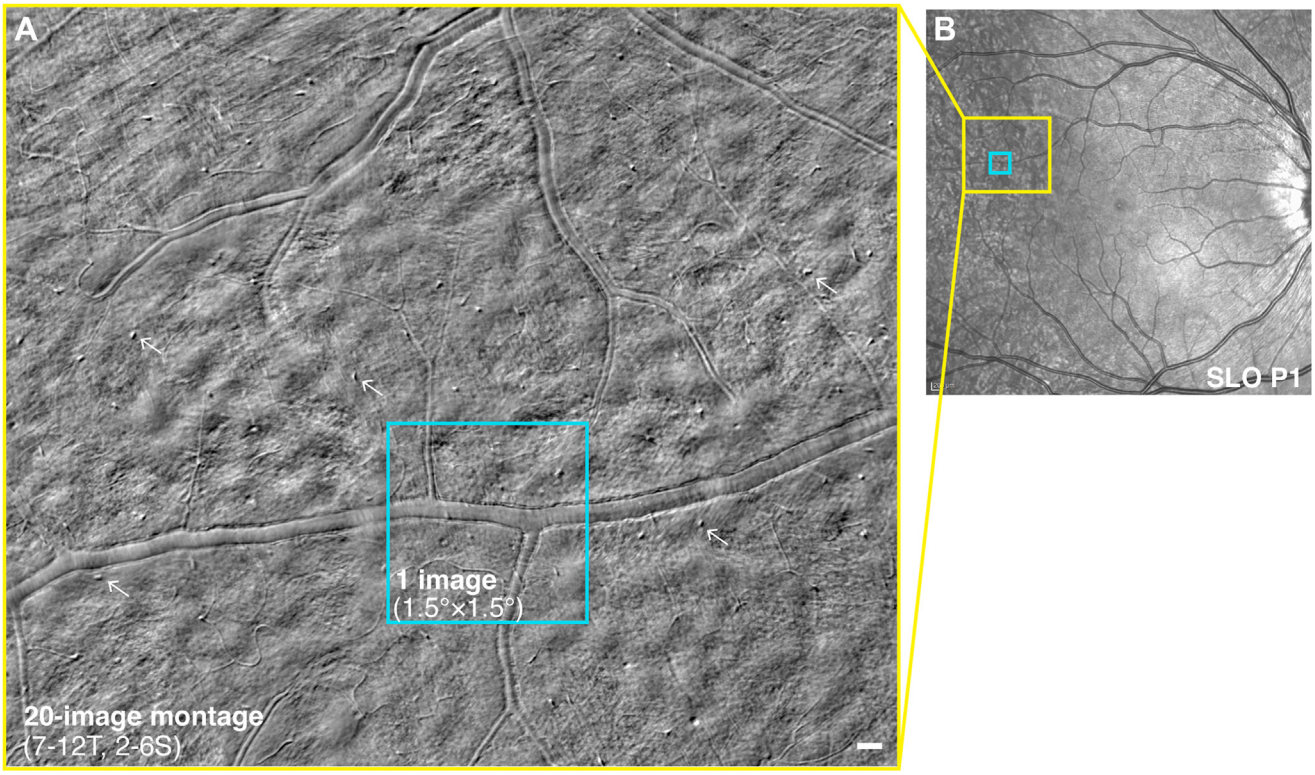

Figure 3. Nonconfocal fiber bundle adaptive optics scanning light ophthalmoscopy (AOSLO) montage showing microglial cells imaged in healthy retina. **A,** Retinal montage composed of 20 images; cyan box denotes the field of view of a single image. White arrows denote 5 example microglial cells (T = temporal, S = superior). Scale bar is 50 μm. **B,** Conventional SLO image for orientation; yellow and cyan boxes correspond to regions marked in (**A**).

A total of 239 presumed microglial cells were detected, segmented, and quantified in 6 healthy eyes (Table S3, available at www.ophthalmologyscience.org). To clearly distinguish potential microglial cell processes from retinal vasculature, we carefully compared FB images to perfusion maps generated through motion contrast processing of the FB data (Fig S4C–D). We hypothesized that ramified microglia in the healthy retina would have lower contrast in the perfusion maps while blood flow will provide a strong motion contrast signal. Yellow arrowheads in Figure S4C–D denote the position of 7 example microglial cells while the pink arrowhead shows 1 putative microglial cell that had both high contrast and was colocalized with a vessel. Though perivascular macrophages are known to reside adjacent to vessels, owing to ambiguity as to whether this was a macrophage or a diving vessel, we conservatively excluded these cells from quantification.

Microglial cells exhibited a spectrum of morphologies (Fig 5) ranging from elongated somas with visible processes to more circular shaped amoeboid somas, resembling ramified and activated microglia, respectively.[29,30] Cell processes were not always detected on the elongated cells suggestive of a ramified appearance. Careful comparison of these cells imaged at different timepoints during a single imaging session reveals the potential for them to extend and retract their processes (see Fig 6A–D and corresponding Video S1, available at www.ophthalmologyscience.org). This illustrates that these morphometric measurements are limited to represent a snapshot in time and that parameters such as the eccentricity (cell circularity) and soma diameter can change dynamically over several minutes.

Microglial cell motility in healthy retinas was manifested in 2 aspects; apart from above mentioned subtle morphological changes (see another example in Video S2, available at www.ophthalmologyscience.org), we also quantified cell soma displacements and calculated their speeds (see example in Fig 6E–G and corresponding Video S3, available at www.ophthalmologyscience.org). Microglial cell speed was measured at 10 different locations in 5 healthy eyes (43 cells in total, Table S4, available at www.ophthalmologyscience.org). In healthy retinas, cell somas moved extremely slowly, with an average speed of 0.02 μm/sec. Microglial cell somas appeared to be mostly static across the timescales we evaluated, with only a few observed to move substantially, at speeds up to 0.13 μm/sec. Cumulative distance is plotted against observation time for 11 cells monitored in P1 in Figure S7 (available at www.ophthalmologyscience.org). Consecutive images were generated across 5 minutes at an interval of 30 seconds. Examples from 0, 3, and 4.5 minutes are shown in Figure S7A–C, and Video S4 (available at www.ophthalmologyscience.org) shows the complete time-lapse animation corresponding to Figure S7A. Cell speed varied between consecutive observation time points, indicating

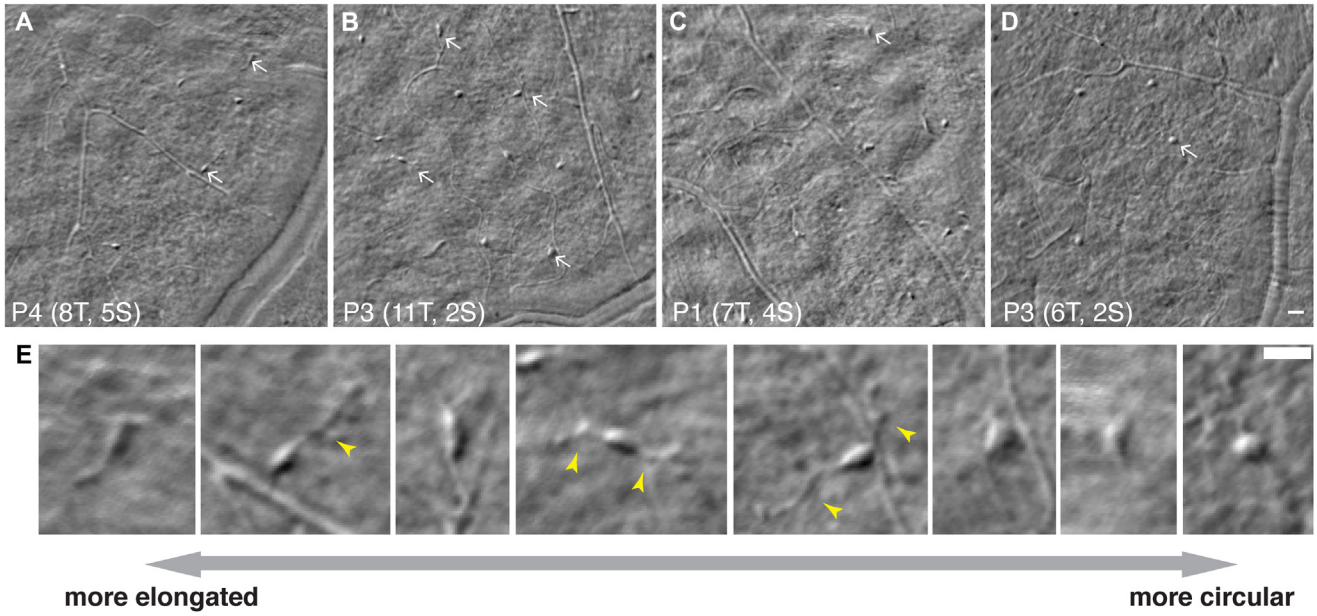

Figure 5. Morphologies of microglial cells visible in healthy retinas. **A–D,** Images from single acquisitions (1.5° × 1.5° field of view); participant number and retinal eccentricity are noted at lower left corner (T = temporal; S = superior). **E,** Examples of presumed microglial cells with different morphologies ranging from more elongated somas to more circular somas, corresponding to cells denoted with white arrowheads in (**A–D**). Yellow arrowheads mark putative microglial cell processes. All scale bars are 25 μm; scalebar in (**D**) applies to (**A–D**).

the uneven speed of these cells that occasionally moved in short bursts (e.g., cell plotted in purple between 2.5 and 3 minutes in Fig S7D). During observation, only 1 cell moved substantially, denoted by the purple line plot shown in Figure S7D (corresponds to cell in purple box in Fig S7A).

The morphometry and motility of microglial cells in healthy retinas are summarized in Tables S3 and S4 and are plotted in Figure 8. A histogram of eccentricity (i.e., circularity) fitted with kernel density estimation for all cells detected across all eyes is shown in Figure 8A. Average soma diameter across all eyes was 16.1 ± 0.9 μm; the histogram in Figure 8B was fit with a normal distribution (mean, 16.27; standard deviation, 2.64). Mean soma diameter was similar in each of the different control eyes, ranging from 14.7–16.96 μm (Table S3). Mean (± standard deviation) soma area for all the cells detected across all eyes was 192.97 ± 17.2 μm^2, and its histogram was plotted and fit with a normal distribution (mean = 194.84; standard deviation, 56.06) in Figure 8C. Average cell density across all 6 participants was 20 cells/mm^2 with large intersubject variability, ranging from 8–28 cells/mm^2 (see Table S3). Cell speeds are plotted in Figure 8D.

Evaluation of Cellular Structures Visible in Patients with Retinal Inflammation from Posterior Uveitis

In a patient's eye (Pt1) diagnosed with acute syphilitic posterior placoid chorioretinitis, many presumed immune cells were observed in the FB images at a first imaging session in the most acute phase of the disease we observed (Fig 9). Six days before imaging, the patient had begun treatment with penicillin (see case details in Table 2). Careful comparison revealed that some of the cells were also barely visible in the confocal channel. Some cells showed morphologies suggestive of macrophages with internal structures; others had more uniform contrast across their extent (Fig 9D). A total of 32 cells, 15.6 μm in diameter, on average, were observed within the imaging field of view.

This location (Fig 10A) was imaged consecutively for 3 minutes (6 videos, 30 seconds each) and then again 12 minutes later (2 videos, 30 seconds each). After registration we averaged 10-second (300 frame) intervals to produce 24 images across the timespan to quantify the speed of the fastest-moving cells within the field of view. Figure 10B shows cell trajectories overlaid on the first nonconfocal FB image with aggregated dots denoting the motion of cells that moved minimally, whereas lines represent cells that traveled longer distances. The trajectories of 5 example cells are highlighted with the positions of cells #1–3 during 40- or 50-second intervals shown in Figure 10C–E. Unlike cell-like structures resembling macrophages that we could detect moving across many images, cells #4 and #5 were serpentine shaped and moved much more rapidly across the field of view. Video S5 (available at www.ophthalmologyscience.org) shows the complete time-lapse video with cells #1–5 marked with the same colors as Figure 10B.

The cumulative distances of these 5 example cells against a 50-second duration are plotted in Figure 10F; for comparison, the gray lines show the speed of several cells detected in healthy participant P1. Figure 10G shows a histogram of the speed of all 32 cells detected in this

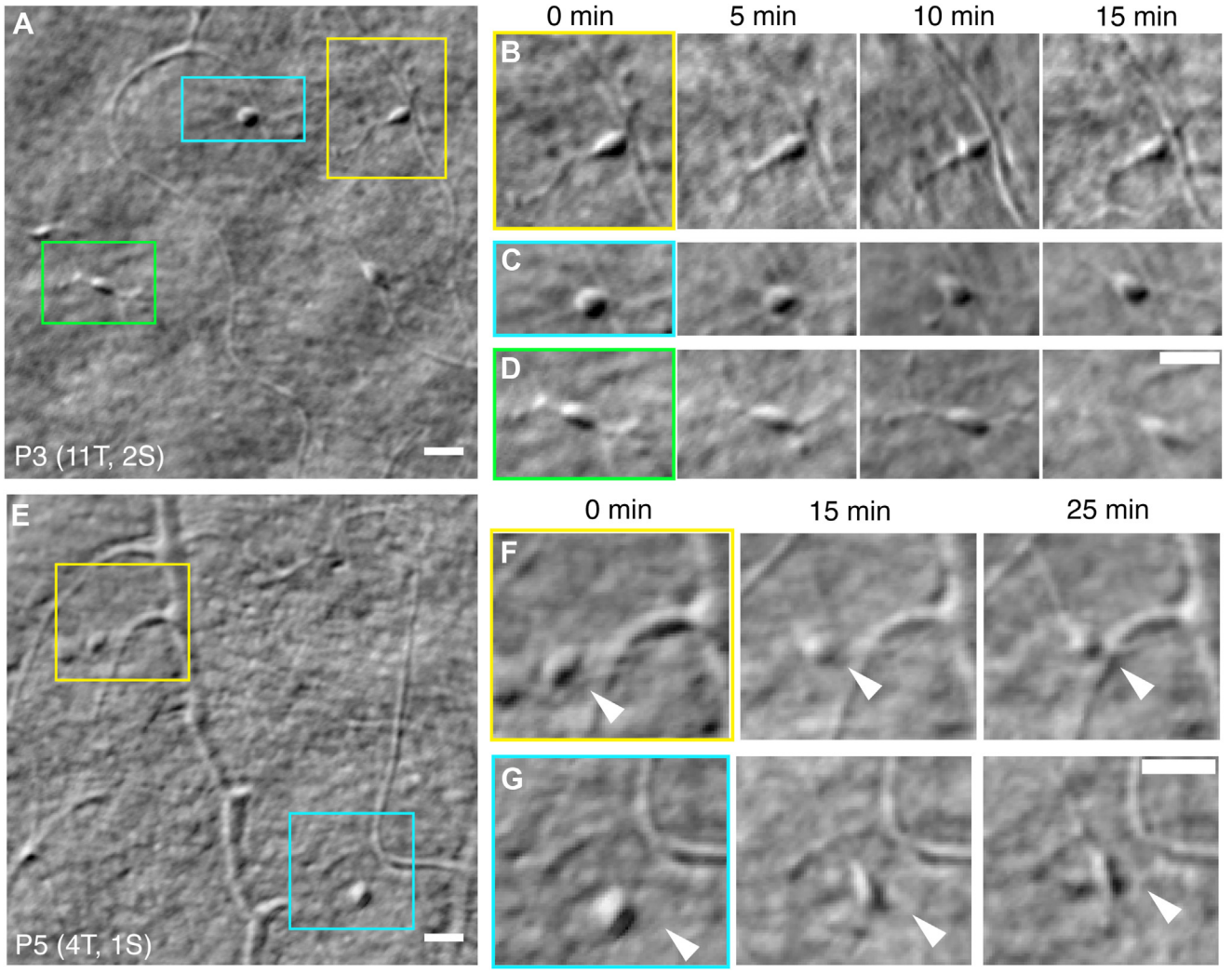

Figure 6. Morphological changes of microglial cells in healthy retinas. **A, E,** Images from single acquisitions (1.5° × 1.5° field of view); participant number and retinal eccentricity are noted at lower left corner (T = temporal; S = superior). Colored boxes are enlarged in (**B**–**D** and **F**–**G**) showing cell position (marked with white arrowheads) at different observation time points. Scale bars are 25 μm for all images.

patient (yellow bars) along with the 43 moving cells quantified in the 5 healthy participants (gray bars). Compared with the slow motion of microglial cells seen in healthy retinas, we observed substantially faster cells in this patient, with speeds up to 3 μm/sec, > 100 times faster than the average speed detected for normal cells. In subsequent imaging at 19 and 34 days later, fewer cells were detected (see day 20 in Video S6 and day 35 in Video S7, available at www.ophthalmologyscience.org), and their average speed was markedly reduced over time (Fig S11, available at www.ophthalmologyscience.org). This reduction in the number and speed of cells was correlated with improvements across other measures including visual acuity, clinical examination findings, and multimodal retinal imaging (Fig S12, available at www.ophthalmologyscience.org).

In patients' (Pt2 and Pt3) eyes diagnosed with noninfectious posterior uveitis, numerous cells and high contrast structures were detected (Fig 13). Many of the cells had similar morphology and size compared with the microglia detected in normal eyes, but we observed many more structures within each field of view compared with normal eyes. Compared with Pt1, cell activity was mostly marked by local morphological changes rather than movement across the field of view. Video S8 (available at www.ophthalmologyscience.org) showed the time-lapse video of the complete observation. Interestingly, though cell motion was apparent in Pt2's eye (Video S8A), with acute retinal vasculitis, it was absent in Pt3's eye (Video S8B), with chronic retinal vasculitis (over 8 years) that was moderately active at the time of imaging. The lack of cell motility in Pt3 suggested that these presumed microglia, at least at the location we imaged, were possibly not in an activated state at the time of imaging. This is interesting to note as clinical retinal imaging in Pt3's eye was not accurate enough to confirm uveitis activity.

As shown in Figure 14, fundus fluorescein angiography (FFA) of Pt3 from 18 and 12 months before the first AOSLO imaging session persistently showed diffuse staining from the retinal vessels due to chronic rupture of

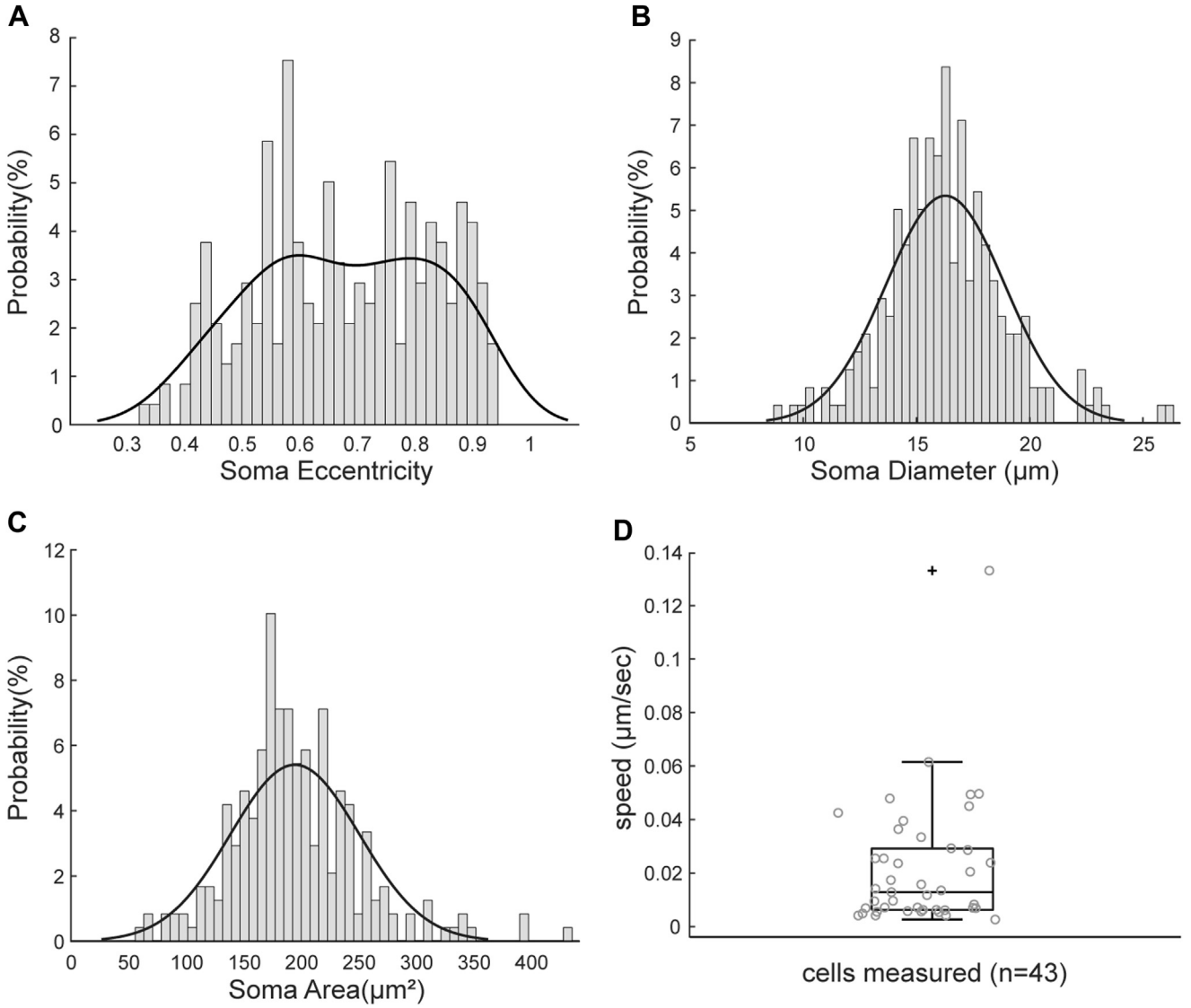

Figure 8. Microglial cell morphometry and speed in healthy retinas. **A,** Histogram of soma eccentricity fit with a kernel density estimation. **B,** Histogram of soma diameter fit with normal distribution (mean = 16.3, standard deviation = 2.6). **C,** Histogram of soma size (represented by soma area) fit with normal distribution (mean = 194.8, standard deviation = 56.1). **D,** Scattered boxplot of speeds for 43 microglial cells from 5 healthy participants.

the blood–retina barrier, making the level of inflammation impossible to assess. Assessment of macular edema, shown on OCT, was used to assist in the clinical evaluation of disease status. The presence of numerous intraretinal cysts at visit 1 on OCT (Fig 15) was suggestive of a moderate level of persisting inflammation that was nearly resolved by visit 2, 16 weeks later (Fig 15C). However, AOSLO taken on the 2 different visits (Fig 15D–G) showed different degrees of high contrast structures in the nonconfocal FB images, including microcysts (Fig 15E, magenta arrowheads), cell-like structures (Fig 15F–G, blue arrows), and numerous small punctate structures of unknown origin (a few denoted with yellow arrows in Fig 15F–G). Interestingly, though microcysts were not clearly seen in the first timepoint in AOSLO, they could be seen with high contrast at visit 2 (Fig 15E, magenta arrowheads). The comparison of AOSLO images between visits agreed with the patient's improvement evaluated from OCT, but the residual cysts, presumed immune cells, and numerous small punctate features seen in images from visit 2 suggested that the posterior uveitis was not fully recovered.

Another example of chronic uveitis is shown in Pt4's eye who had chronic uveitis for $>$ 20 months and received treatments for macular edema that was resolved at the time of imaging. Adaptive optics scanning light ophthalmoscopy images from this patient's eye (Fig S16, available at www.ophthalmologyscience.org) showed almost no macrophage-like cells, consistent with the quiescent state of uveitis at that time. Taken together, the results from imaging these patients demonstrate the potential for improving the evaluation of uveitis by revealing fine-scale dynamic structural changes, especially in cases where

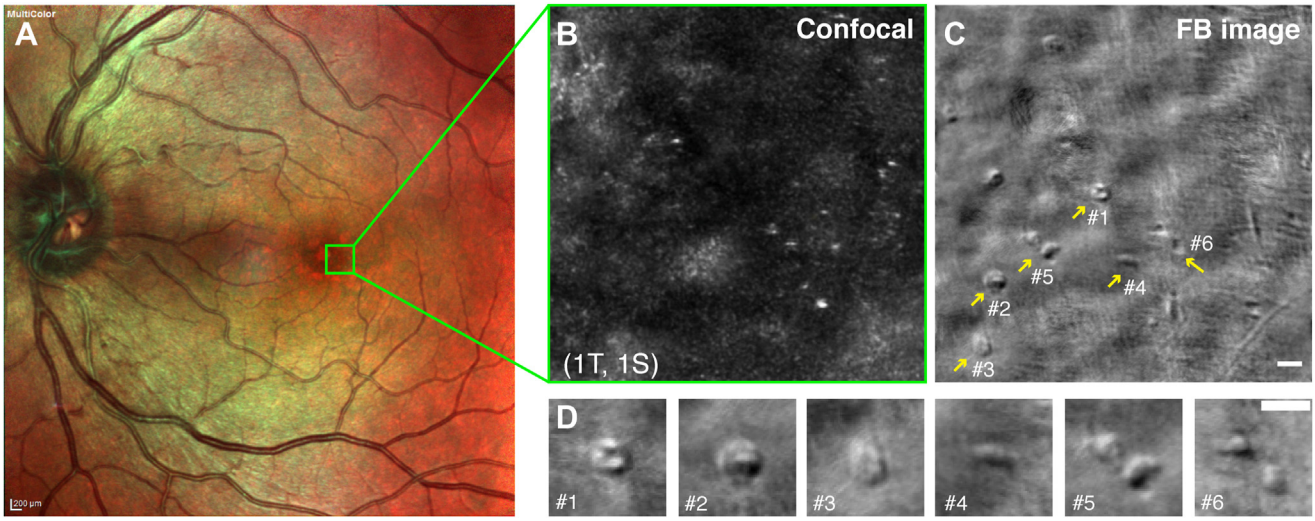

Figure 9. Inflammatory cells with macrophage-like appearance imaged in patient 1 with acute syphilitic posterior placoid chorioretinitis. **A,** Multicolor-mode fundus photo revealed granular dots within the foveal area; green box denotes foveal region imaged with adaptive optics scanning light ophthalmoscopy. **B,** confocal and (**C**) nonconfocal fiber bundle (FB) images. Numbered yellow arrowheads denote some example cells that are enlarged to show detail and variability in morphology in (**D**). Scale bars are 25 µm for (**B**–**D**). S = superior; T = temporal.

conventional clinical imaging showed difficulty in determining disease status.

Discussion

In this current study, we showed that individual cells, presumably microglia and macrophages, can be directly imaged, and their morphology and dynamic activity quantified in the living eye of patients with uveitis using existing AOSLO instrumentation with only minor modifications. To our knowledge, this is the first time that presumed retinal microglia and macrophage-like cells and their motility have been imaged and quantified during active infections or inflammations in the living human eye. The capability to image immune cells within the retina and track their activity longitudinally could be transformative for future studies, as microglia and macrophages play a prominent role in the pathophysiology of numerous retinal diseases.[31] More work is still needed to refine this tool for clinical use, but we have demonstrated here that the technological improvements afforded through simultaneous multioffset detection using a FB are a major step forward, reducing the acquisition time substantially and allowing for fine-scale tracking of changes over time. Similar nonconfocal approaches with sensitivity to detect microglia, such as nonconfocal quadrant detection, should also have the sensitivity to detect immune cells in patients with inflammation.

Future work should evaluate the efficacy of nonconfocal imaging for detecting inflammatory cells at different stratifications within the retina. In our earlier studies in monkeys we showed multioffset detection was capable of fine-scale axial sectioning,[24] and we hypothesize here that we are imaging cells near the ganglion cell layer. However, we cannot rule out that we are not also detecting cells that reside on the surface of the retinal nerve fiber layer and focus can be challenging to maintain at the exact same axial position in AOSLO, especially when imaging the optic nerve head or areas near pathology where retinal thickness changes rapidly over short spans. Since we saw much more detail in our images of inner retinal structures (e.g., retinal ganglion cells, superficial vessels, and axon bundles) than was shown in the images of Migacz et al[14] that were hypothesized to be the vitreous cortex hyalocytes, we suspect that we are imaging at a deeper focal plane. We also did not detect structures resembling the web-like pattern that they showed in the background of their images that they hypothesized to be the vitreous cortex. It is notable that the processes of the cells they detected appeared more visible in most cases, possibly since the cells on the vitreous have fewer surrounding structures that could obscure them. Since we used a different optical setup and image processing approach, more work is needed to fully understand the differences between our images and theirs. We plan in future investigations to compare the cells we can detect to those seen on OCT[32] and evaluate the efficacy of our approach for detecting immune cells through the full thickness of the retina.

Microglia imaged in healthy retinas showed a spectrum of morphologies, including rounded cells and elongated cells with visible processes, consistent with histological studies that have shown ramified parenchymal microglia having characteristics of dendritic antigen-presenting cells and perivascular macrophages around blood vessels similar to macrophages of the mononuclear phagocyte series.[33,34] This is consistent with the histogram of segmented cell eccentricities shown in Figure 8A that shows a range of eccentricity values corresponding to a range of segmented shapes spanning from more elliptical to more circular cells. The fit applied to Figure 8A is suggestive of a bimodal distribution of cell shapes which could be interpreted as 2 overlapping cell populations, one more

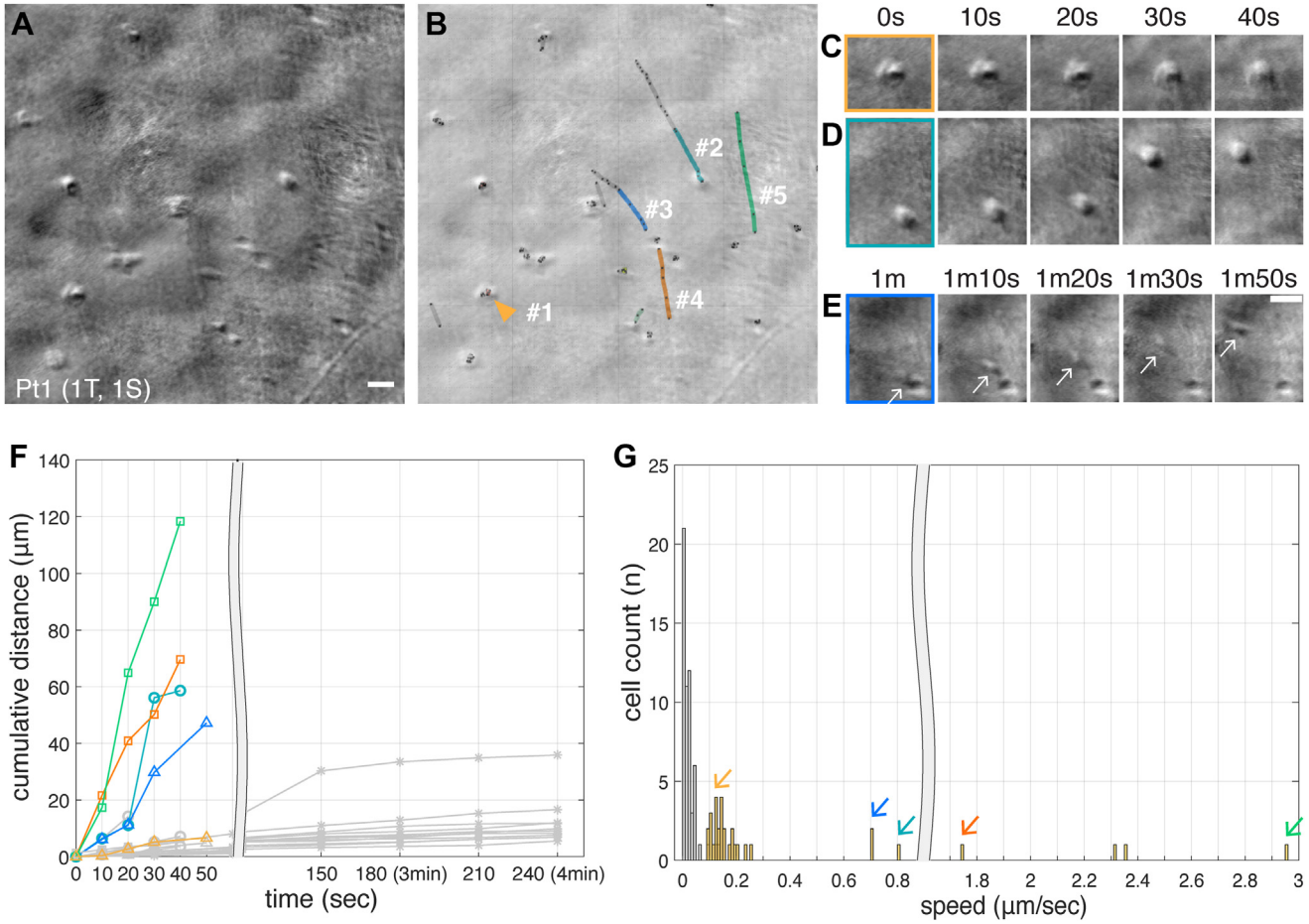

Figure 10. Cell motility of patient 1 (Pt1). **A,** The first image during observation. Scale bar is 25 µm. **B,** Cell position track plot superimposed onto a semitransparent version of (**A**) to highlight cell trajectory. Lines and aggregated dots show cell positions throughout the entire observation. Nine example cells are marked with numbers and yellow asterisk. Positions of cells marked with yellow arrowhead, #1, and #2 are enlarged in (**C**–**E**) showing their position during a 40-second (or 50-second) duration, respectively. Scale bar in (**E**) is 25 µm and applies to images (**C**–**E**). **F,** The cumulative distance of selected cells against 50-second duration during the entire observation. Gray lines represent 11 example cells detected in healthy retinas including the cell that moved the fastest. **G,** Histogram of the speed of all 32 cells detected from Pt1 during the entire observation (yellow bars) and all 43 cells detected from 5 healthy participants (gray bars). Color arrowheads match numbered cells in (**B**). S = superior; T = temporal.

circular and the other more elliptical. However, since we are imaging 3-dimensional structures with an en face imaging modality, the cross section of each cell that we detect depends on the orientation of the cell with respect to the plane of the retina (and imaging). Though there is little data in the literature on the morphometric properties of human retinal microglial cell somas, a previous histological study showed that human retinal microglial cell bodies were irregular in shape, measuring 5–10 µm in the short axis and 10–15 µm in the long axis;[35] this is consistent with the soma sizes we measured here that are plotted in Figure 8B. Therefore, if we assume the cells we imaged are ellipsoids oriented randomly, we should expect to see a range of eccentricity values. This same issue presents some uncertainty in our ability to evaluate changes in cell morphology over time. For example, for the cells that appeared more circular, it is possible that we detected them in a certain orientation that made them appear more circular or only captured a part of their somas that appeared circular. We also suspect that we were not able to visualize all the processes of each cell, particularly those that may have been oriented axially with respect to our en face imaging modality. These issues are not unique to AOSLO and it has been previously shown that obtaining accurate morphometric measurements of microglial cells is challenging in other imaging modalities.[29]

Cell motion differed markedly between active posterior uveitis and healthy eyes without inflammation. Cells moved slowly in normal eyes (0.02 µm/sec on average, 0.13 µm/sec maximum), but could move at speeds > 100 times the normal average in eyes with active inflammation secondary to infection (e.g., Pt1). Interestingly, we were able to detect some of the same cells at all 3 visits (marked with colored arrowheads in Fig S11A, C, E), but the fastest-moving structures were only clearly seen in the first timepoint in the most acute stage we evaluated and on the second visit, just during the first 30 seconds. The cells with the highest speeds we detected (cells #4 and #5 in Fig 10B) were

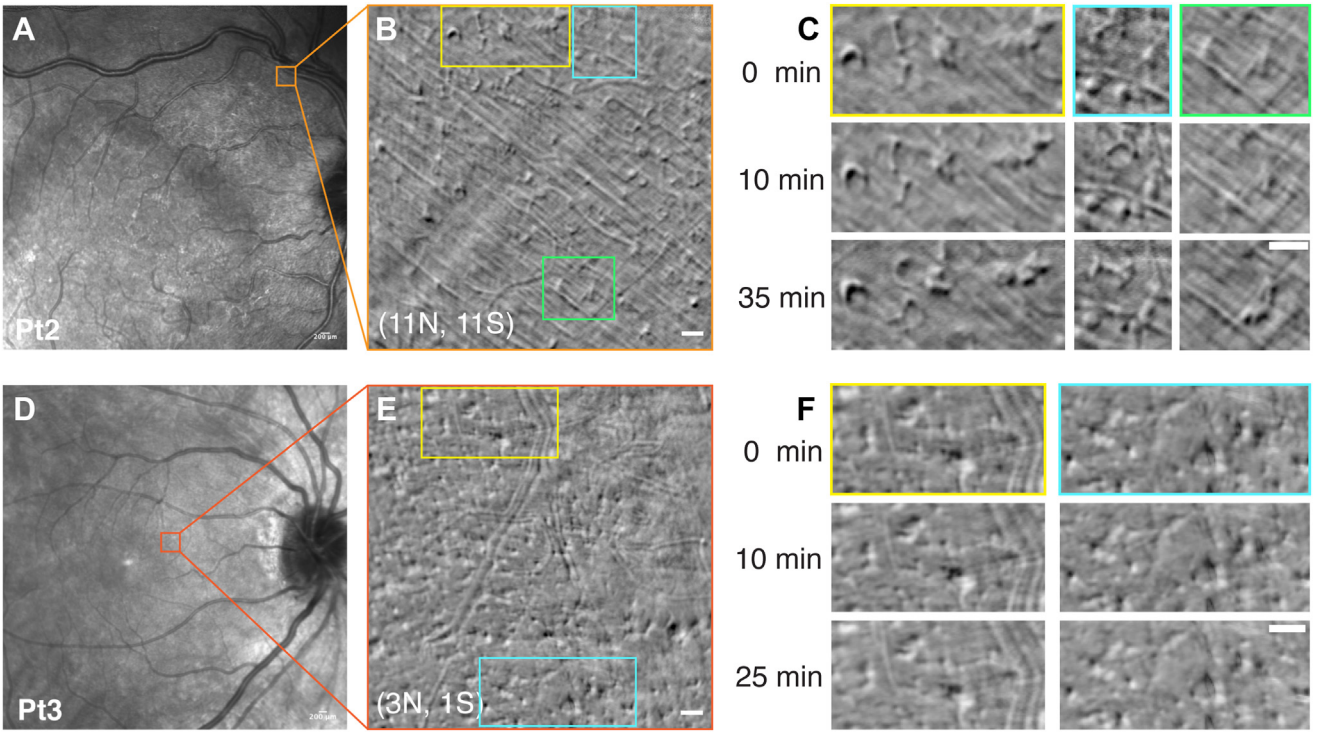

Figure 13. Cellular structures visible in patients with active (patient [Pt]2) versus chronic quiescent (Pt3) uveitis. **A, D,** Conventional scanning light ophthalmoscopy (SLO) images of Pt2 and Pt3, respectively. Orange-colored boxes denote retinal location imaged with adaptive optics SLO shown in **(B, E)**. Scale bars are 20 μm. Colored boxes in **(B)** and **(E)** denote locations enlarged in **(C, F)** to show detail of cells and cell-like structures visible across 3 different observation time points. Scale bars in **(C, F)** are 20 μm. N = nasal; S = superior.

serpentine in shape and we hypothesize that these were either immune cells that were moving too fast for our detection rate, causing them to appear stretched due to insufficient temporal sampling (i.e., motion blur), or that they may conceivably represent detection of individual *Treponema pallidum* bacteria, the organisms that cause syphilis.

However, because the bacteria are smaller than the resolution limit of our imaging system in 1 dimension (the literature reports that spirochaetes of *T. pallidum* are 10 to 20 μm in length but only 0.1 to 0.2 μm wide, on average[36,37]), it is conceivable that they could be *detected*, but if they were they would not be rendered at their actual size but would appear artificially enlarged. This is because when objects smaller than the optical point spread function of an imaging system are detected, they will appear to be the size of the system point spread function. Measurements of cells #4 and #5 from Pt. 1 in Figure 10 show them to be ∼ 18 and ∼ 36 μm in length, respectively, and ∼ 5 micrometers in diameter. The shorter one is close to the expected length of *T. pallidum* but both are much greater in width. It is possible that this is still perhaps within the ballpark of what we might expect for these structures in AOSLO, since they could potentially be blurred by the system point spread function and residual optical aberrations and also be blurred due to motion from insufficient temporal sampling, but this is highly speculative and requires further study. Spirochaetes such as *T. pallidum* have different morphometric properties than other infectious organisms, so if it is possible to effectively detect them, it may be possible through in vivo imaging to detect other types of bacteria with different morphometric properties or potentially other organisms, such as parasites, using nonconfocal AOSLO. Some of the structures visible in the patients with noninfectious uveitis did not look like macrophages and exhibited characteristics that require further study. More work is needed to evaluate the effectiveness of detection for other structures beyond microcysts, macrophages, and microglia.

Our approach is simpler to implement optically in existing systems than other phase contrast methods that have been demonstrated in AOSLO. Mozaffari et al[28] demonstrated the feasibility of optical FB detection for AOSLO using an off-the-shelf FB in a flexible setup for either pixel reassignment or multioffset detection. Here we used a custom detection pattern and implemented it in a less flexible but much simpler optical setup that requires no additional optics, such as the mask and extra telescope they required.[28] Our approach is also simpler to implement than a related technique that also achieves sensitivity to phase across multiple angles, nonconfocal quad detection, which requires 18 additional optical elements to be added and precisely aligned for implementation.[25] The present method could easily be implemented optically in existing AOSLO systems with only the focal length of the final lens (or FB geometry) needing to be adapted appropriately.

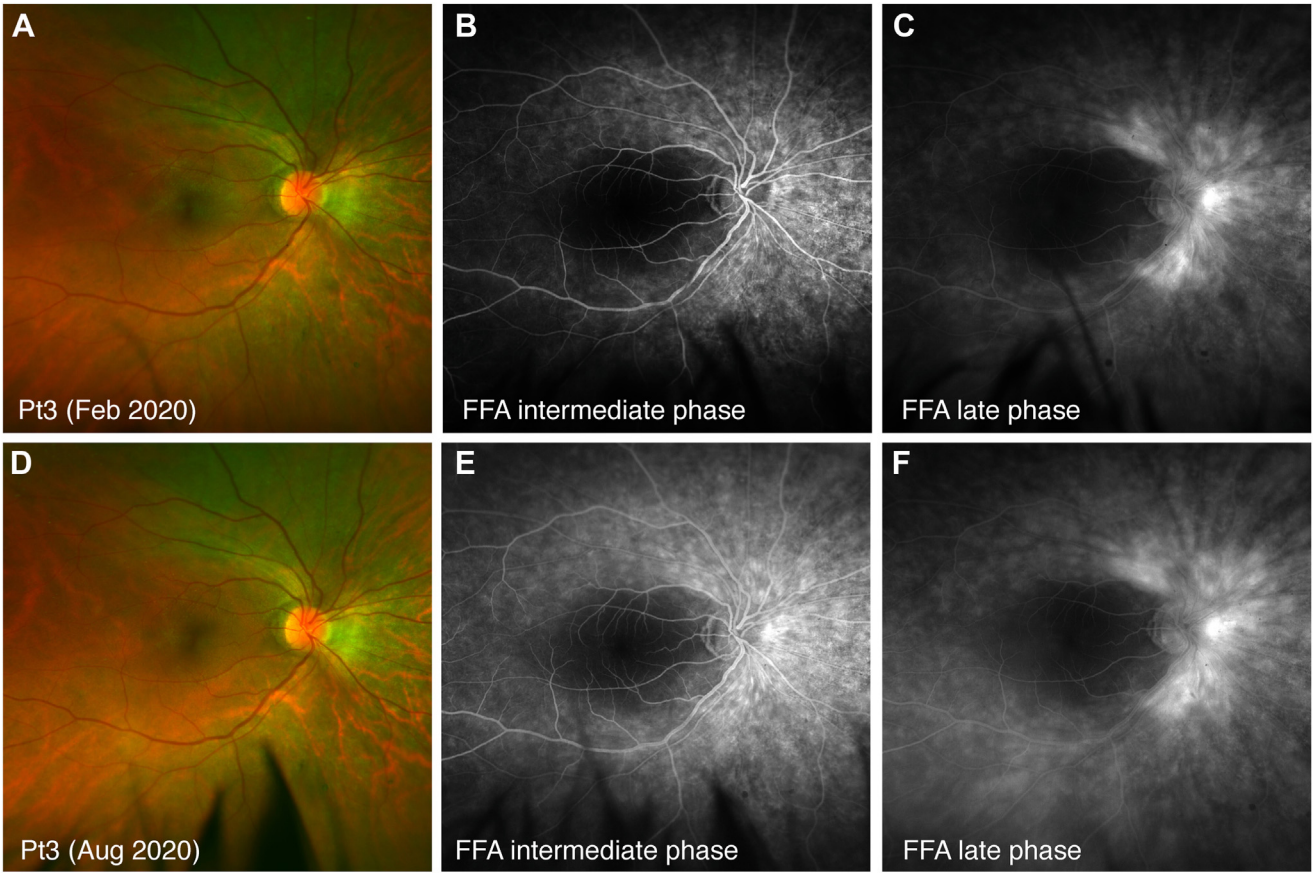

Figure 14. Fundus photo and fundus fluorescein angiography (FFA) of patient (Pt)3. **A–C,** Images acquired 18 months prior to her first adaptive optics scanning light ophthalmoscopy (AOSLO) imaging session. Fundus fluorescein angiography showed widespread retinal fluorescein staining. Size of the hyperfluorescent areas remained the same between early and late phases. **D–F,** Images acquired 12 months prior to her first AOSLO imaging session. Fundus fluorescein angiography showed unchanged fluorescein retinal staining.

Nonconfocal AOSLO imaging of mice has allowed label-free imaging of microglia and their motility.[38,39] Investigations in mice have used fluorescent markers to differentiate resident microglia from infiltrating immune cells in an endotoxin induced uveitis model[40] where heterogenous immune cells, neutrophil, and monocyte populations and their motility were imaged. Neutrophils were seen rolling along the venular endothelium and infiltrating monocytes and macrophages were present both in vessels and extravasated into retinal tissue.[40] A limitation for human imaging is that we do not presently have the capability to selectively label cells to differentiate activated resident microglia from infiltrating macrophages. However, this previous work showed images that look strikingly similar to what we observed here in patients with uveitis, particularly the macrophage-like cells with granular internal structures seen in Pt1's eye with acute syphilitic posterior placoid chorioretinitis.

Current clinical imaging modalities for managing posterior uveitis and determining the level of inflammatory activity include FFA, fundus autofluorescence, and OCT.[41,42] A few case-reports and small case series have studied the photoreceptor layer and vasculature changes in uveitis with adaptive optics ophthalmoscopy but immune cells have not previously been studied.[43–45] Uveitis treatment involves therapeutic immunomodulatory strategies that may be categorized into those that modulate the general activation state of microglia, like corticosteroids, and those that modulate specific molecular pathways through which microglia exert pathologic effects.[3] Local retinal delivery of corticosteroids has demonstrated significant suppressive effects on microglial cell activation.[46] In a case of chronic noninfectious uveitis on immunomodulatory treatment (Pt3), cell motility was imperceptible, likely due to the steroids the patient was receiving. We also saw only a few putative microglia in a patient with chronic posterior uveitis and recent resolved macular edema 2 months after intravitreal steroids injection (Pt4, Fig S16). This suggests that nonconfocal phase contrast AOSLO methods may be useful for monitoring the efficacy of immunomodulatory therapies in uveitis especially in cases of chronic uveitis. In cases of chronic (long-term) conditions or in those with many relapsing episodes, FFA interpretation cannot always ascertain the level of uveitis activity or quiescence because of similar angiographic features between chronic quiescent retinal staining and acute active fluorescein leakage. Fundus fluorescein angiography remains the gold standard to diagnose the level of activity of posterior uveitis but FFA

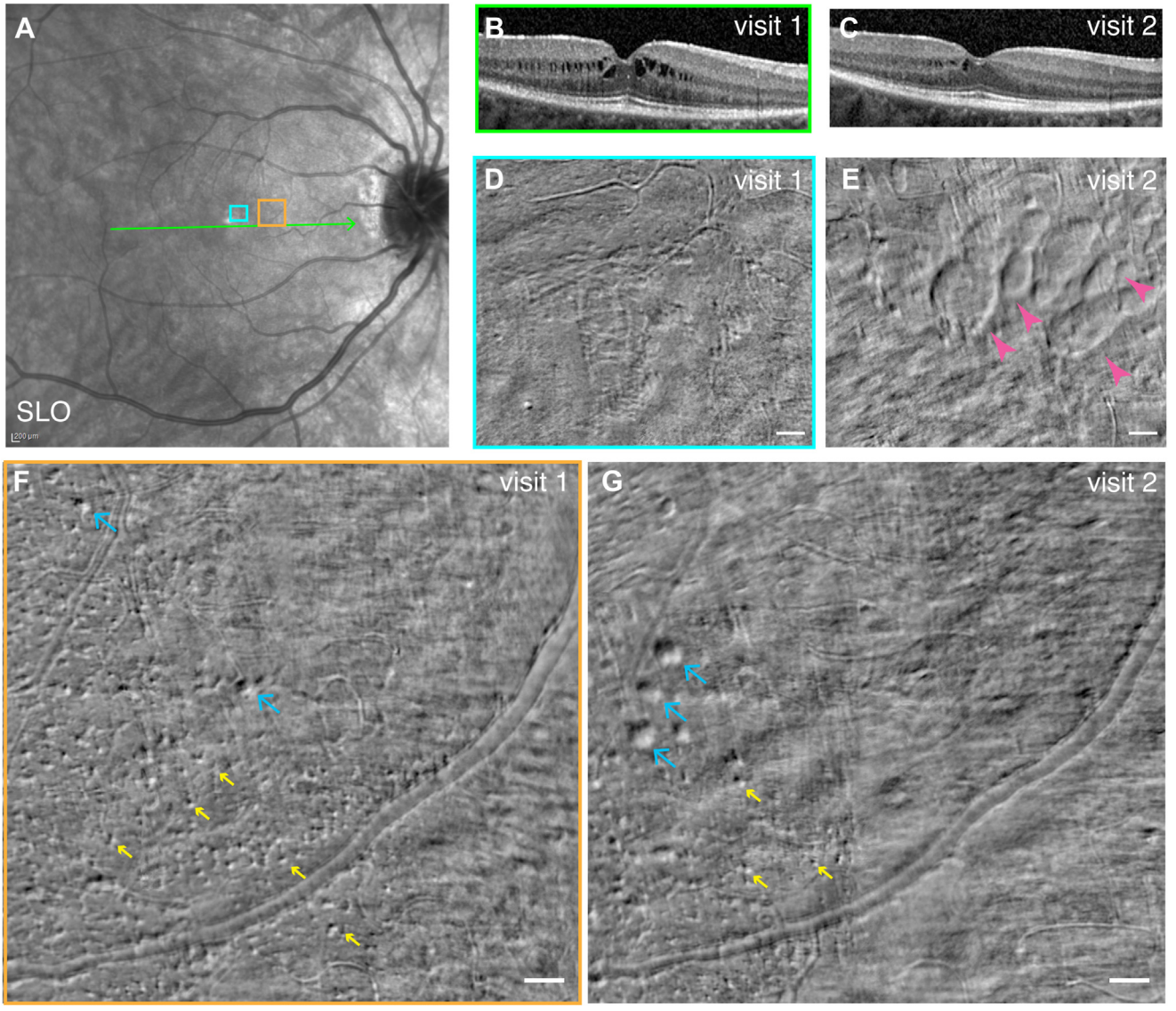

Figure 15. Longitudinal imaging of patient 3 with chronic retinal vasculitis showing substantial changes over time. **A,** Conventional scanning light ophthalmoscopy (SLO); green line marks OCT B-scan positions shown in (**B**) and (**C**). Cyan and orange boxes denote locations imaged at each timepoint. OCT scans (**B, C**) showed fewer intraretinal cysts were visible clinically at the second timepoint. **D, E,** Nonconfocal adaptive optics SLO montages of 4 single-acquisition images of a retinal region near the fovea showed microscopic-scale intraretinal cysts were visible at the second timepoint that were not apparent at this region at the first image timepoint, contrary to expectations from the clinical data. Magenta arrowheads in (**E**) denote a few of the larger microcysts. **F–G,** Montage of 4 images of the affected region with numerous cell-like structures visible at both timepoints; the blue arrows point to cell-like structures that we hypothesize may be macrophages and the yellow arrows point to tiny punctate structures. Scale bars are 50 μm.

remains a subjective imaging test based on the ophthalmologist's interpretation.

Objective measures of intraocular inflammation are still a matter of current research for posterior uveitis. The amount of leakage in retinal vasculitis has been studied recently with development of automated leakage analysis using wide field fluorescein angiograms in uveitis patients. Those studies focus on automated processing techniques for standardization and normalization of FFA images in patients with uveitis.[47] For retinal and choroidal lesions, autofluorescence and en face fundus images are now used in clinical trials to assess the level of inflammation. Other markers of inflammation used in clinical practice include macular edema, cells in vitreous, and vascular sheathing. Better grading is essential for assessing disease status and treatment efficacy. Improved clinical imaging tools for in vivo visualization of retinal inflammation are currently needed to provide objective and quantitative proof of active versus quiescent ocular inflammation. Nonconfocal AOSLO imaging of immune cells and their dynamics in

patients may allow for better understanding of various retinal diseases and help reveal disease severity quantitatively. Though imaging is challenging in the presence of media opacities such as vitritis or cataract, it offers the unique possibility of quantifying the detailed dynamic features of individual cells in posterior uveitis when the media is clear enough for imaging.

Considering future use of nonconfocal AOSLO as a tool for studying uveitis, there are considerable challenges in terms of the quantification of the approach and improvements are needed to replace the manual procedures used here for quantification with automated methods for cell detection and tracking. Additional work is also required to identify the structures seen in these images that cannot be identified presently, such as the fast-moving structures previously described from Pt1, the dynamic structures seen in Pt2, and the small punctate features seen in Pts. 2–4. Another limitation of this approach for imaging uveitis is that it will only be useful in posterior uveitis patients that do not have substantial vitritis or media opacities. However, even in its present form, nonconfocal AOSLO may give considerable insight into the pathogenesis of posterior uveitis.

In conclusion, this simplified optical design for nonconfocal multioffset detection using a custom FB can improve the efficiency for nonconfocal phase contrast imaging in AOSLO. Using this setup, we characterized the fine-scale structure and motility of presumed microglia in healthy retinas. We also showed that the morphology and dynamics of presumed immune cells and putative macrophages can be quantified in the living eyes of patients affected by uveitis and active infections. Fiber bundle-based multioffset detection in AOSLO offers promise as a powerful tool to evaluate disease status (i.e., active or quiescent) and response to treatment in uveitis, the third-leading cause of preventable blindness worldwide,[48] both clinically and in future trials. Nonconfocal FB-AOSLO also holds substantial potential for evaluating other blinding conditions where inflammation, macrophages, and microglia play an important role such as glaucoma, optic neuritis, inherited retinal degenerations, and age-related macular degeneration.

Footnotes and Disclosures

Originally received: May 25, 2023.
Final revision: December 22, 2023.
Accepted: January 16, 2024.
Available online: January 20, 2024.Manuscript no. XOPS-D-23-00114R1.

[1] Department of Ophthalmology, University of Pittsburgh School of Medicine Pittsburgh, Pennsylvania.

[2] Eye Center of Xiangya Hospital, Central South University Hunan Key Laboratory of Ophthalmology Changsha, Hunan, China.

[3] Department of Bioengineering, University of Pittsburgh Swanson School of Engineering Pittsburgh, Pennsylvania.

[4] Sorbonne Université, INSERM, CNRS, Institut de la Vision, Paris, France.

[5] CHNO des Quinze-Vingts, INSERM-DGOS CIC 1423, Paris, France.

[6] Institut Langevin, ESPCI Paris, Université PSL, CNRS, Paris, France.

[7] Department of Ophthalmology, University of Pittsburgh School of Medicine, Pittsburgh, Pennsylvania.

[8] School of Optometry, University of California, Berkeley, California.

[9] McGowan Institute for Regenerative Medicine Pittsburgh, Pennsylvania.

Disclosures:

All authors have completed and submitted the ICMJE disclosures form.

The author(s) have made the following disclosure(s):

Y.R.: Support – visiting scholar program of Xiangya School of Medicine, CSU, PRC.

E.G.S: Support – University of Pittsburgh.

K.G.: Support – Foundation Fighting Blindness (PPA-0819-0772-INSERM).

J.A.S.: Support – Laboratoire d'Excellence (LabEx) LIFESENSES (ANR-10-LABX-0065), Institut Hospitalo-Universitaire FOReSIGHT (ANR-18-IAHU-0001), LIGHT4DEAF (ANR-15-RHUS-000), The Edward N. & Della L. Thome Memorial Foundation Awards Program in Age-Related Macular Degeneration Research, United States Department of Defense (W81XWH-22-9-0011 & 2019-447-005), NIH National Institutes of Health, CORE Grant (P30 EY08098), RPB Research to Prevent Blindness, Unrestricted Grant, European Research Council (ERC) Synergy Helmholtz Grant (#610110); Royalties or licenses – patents on allotopic expression relevant to gene therapy of Leber hereditary Optic neuropathy; Consulting fees – AVISTA RX; Patents – portfolio on rod-derived-cone viability factor, optogenic therapy; Leadership or fiduciary role – unpaid censor on the board of Gensight, Sparing Vision, censor on the board of AVISTA, chair advisory board of Sparing Vision, Tenpoint, Institute of Ophthalmology, Basel, president of Foindation Voir et Entendre, director, board of trustees, RD fund (Foundation Fighting Blindness), Gilbert Foundation; Stock or stock options – Pixium Vision, GenSight Biologics, Sparing Vision, Prophesee, Chronolife, Tilak Healthcare, VegaVect Inc., AVISTA, Tenpoint, SharpEye.

M.H.E.: Support – This work was supported by NIH CORE Grant P30 EY08098 to the Department of Ophthalmology, the Eye and Ear Foundation of Pittsburgh, and from an unrestricted grant from Research to Prevent Blindness, New York, NY. This work was supported by NIH CORE Grant P30 EY08098 to the Department of Ophthalmology, the Eye and Ear Foundation of Pittsburgh, and from an unrestricted grant from Research to Prevent Blindness, New York, NY.

E.A.R.: Support – Foundation Fighting Blindness (PPA-0819-0772-INSERM), BrightFocus Foundation (G2017082), National Eye Institute (R01EY030517), departmental startup funds from the University of Pittsburgh, National Eye Institute Core Grant for Vision Research P30 (EY08098), Eye and Ear Foundation of Pittsburgh, Research to Prevent Blindness, New York, N.Y. USA, visiting scholar program of Xiangya School of Medicine, CSU, PRC; Honoraria – honorarium for giving a remotely presented lecture at the 4th Xiangya International Forum of Ophthalmology on 11/26/22; Travel support – Robotrak Technologies Inc.; Patents – (US10,772,496; US10,123,697; & US10,092,181).

The other authors have no proprietary or commercial interest in any materials discussed in this article.

Supported by the Foundation Fighting Blindness (PPA-0819-0772-INSERM), BrightFocus Foundation (G2017082), National Eye Institute (R01EY030517), departmental startup funds from the University of Pittsburgh (to E.A.R.), National Eye Institute Core Grant for Vision Research (P30EY08098) to the University Pittsburgh Department of Ophthalmology, Eye and Ear Foundation of Pittsburgh, Research to Prevent Blindness, visiting scholar program of Xiangya School of Medicine, CSU, PRC. The sponsor or funding organization had no role in the design or conduct of this research.

This work was presented as a poster at the 2022 annual meeting of the Association for Research in Vision and Ophthalmology (ARVO), May 1−4, 2022, Denver, Colorado.

HUMAN SUBJECTS: Human subjects were included in this study. This study was approved by the Institutional Review Board of the University of Pittsburgh and adhered to the tenets of the Declaration of Helsinki. Written informed consent was acquired before enrollment for each participant following a detailed explanation of experimental procedures both verbally and in writing. Written informed consent included potential use of participants' deidentified ophthalmology examination results.

No animal subjects were used in this study.

Author Contributions:

Conception and design: Rui, Gofas-Salas, Mecê, Tiruveedhula, Grieve, Sahel, Errera, Rossi

Data collection: Rui, Lee, Zhang, Snyder, Raghuraman, Yadav, Tiruveedhula, Rossi

Analysis and interpretation: Rui, Lee, Zhang, Snyder, Raghuraman, Mecê, Yadav, Grieve, Sahel, Errera, Rossi

Obtained funding: Rossi, Grieve

Overall responsibility: Rui, Grieve, Errera, Rossi

Abbreviations and Acronyms:
AOSLO = adaptive optics scanning light ophthalmoscopy; **FB** = fiber bundle; **FFA** = fundus fluorescein angiography; **P** = participant; **Pt** = patient.

Keywords:
Adaptive optics, Retinal microglia, Macrophage, Uveitis, Inflammation.

Correspondence:
Ethan A. Rossi, PhD, Department of Ophthalmology, University of Pittsburgh School of Medicine, UPMC Vision Institute at Mercy Pavilion, 1622 Locust St., Room 8.396, Pittsburgh. PA 15219. E-mail: rossiea@pitt.edu.

References

1. Kettenmann H, Hanisch UK, Noda M, Verkhratsky A. Physiology of microglia. *Physiol Rev*. 2011;91:461−553.
2. Langmann T. Microglia activation in retinal degeneration. *J Leukoc Biol*. 2007;81:1345−1351.
3. Silverman SM, Wong WT. Microglia in the retina: roles in development, maturity, and disease. *Annu Rev Vis Sci*. 2018;4:45−77.
4. Wang X, Zhao L, Zhang J, et al. Requirement for microglia for the maintenance of synaptic function and integrity in the mature retina. *J Neurosci*. 2016;36:2827−2842.
5. Singaravelu J, Zhao L, Fariss RN, et al. Microglia in the primate macula: specializations in microglial distribution and morphology with retinal position and with aging. *Brain Struct Funct*. 2017;222:2759−2771.
6. Roubeix C, Dominguez E, Raoul W, et al. Mo-derived perivascular macrophage recruitment protects against endothelial cell death in retinal vein occlusion. *J Neuroinflammation*. 2019;16:157. https://doi.org/10.1186/s12974-019-1547-8.
7. Mendes-Jorge L, Ramos D, Luppo M, et al. Scavenger function of resident autofluorescent perivascular macrophages and their contribution to the maintenance of the blood−retinal barrier. *Invest Ophthalmol Vis Sci*. 2009;50:5997−6005.
8. Hammer DX, Agrawal A, Villanueva R, et al. Label-free adaptive optics imaging of human retinal macrophage distribution and dynamics. *Proc Natl Acad Sci*. 2020;117:30661−30669.
9. Chen L, Yang P, Kijlstra A. Distribution, markers, and functions of retinal microglia. *Ocul Immunol Inflamm*. 2002;10:27−39.
10. Gordon S, Plüddemann A, Martinez Estrada F. Macrophage heterogeneity in tissues: phenotypic diversity and functions. *Immunol Rev*. 2014;262:36−55.
11. Janeway CA, Medzhitov R. Innate immune recognition. *Annu Rev Immunol*. 2002;20:197−216.
12. Liyanage SE, Gardner PJ, Ribeiro J, et al. Flow cytometric analysis of inflammatory and resident myeloid populations in mouse ocular inflammatory models. *Exp Eye Res*. 2016;151:160−170.
13. Gofas-Salas E, Rui Y, Mecê P, et al. Design of a radial multi-offset detection pattern for in vivo phase contrast imaging of the inner retina in humans. *Biomed Opt Express*. 2022;13:117−132.
14. Migacz JV, Otero-Marquez O, Zhou R, et al. Imaging of vitreous cortex hyalocyte dynamics using non-confocal quadrant-detection adaptive optics scanning light ophthalmoscopy in human subjects. *Biomed Opt Express*. 2022;13:1755−1773.
15. Roorda A, Duncan JL. Adaptive optics ophthalmoscopy. *Annu Rev Vis Sci*. 2015;1:19−50.
16. Roorda A, Romero-Borja F, Donnelly III W, et al. Adaptive optics scanning laser ophthalmoscopy. *Opt Express*. 2002;10:405−412.
17. Pircher M, Zawadzki RJ. Review of adaptive optics OCT (AO-OCT): principles and applications for retinal imaging [invited]. *Biomed Opt Express*. 2017;8:2536−2562.
18. Liang J, Williams D, Miller D. Supernormal vision and high-resolution retinal imaging through adaptive optics. *J Opt Soc Am*. 1997;14:2884−2892.
19. Liu Z, Kocaoglu OP, Miller DT. 3D imaging of retinal pigment epithelial cells in the living human retina. *Invest Ophthalmol Vis Sci*. 2016;57:OCT533−OCT543.
20. Liu Z, Kurokawa K, Zhang F, et al. Imaging and quantifying ganglion cells and other transparent neurons in the living human retina. *Proc Natl Acad Sci U S A*. 2017;114:12803−12808.
21. Chui TYP, VanNasdale DA, Burns SA. The use of forward scatter to improve retinal vascular imaging with an adaptive optics scanning laser ophthalmoscope. *Biomed Opt Express*. 2012;3:2537−2549.
22. Elsner A, Miura M, Burns S, et al. Multiply scattered light tomography and confocal imaging: detecting neovascularization in age-related macular degeneration. *Opt Express*. 2000;7:95−106.
23. Scoles D, Sulai YN, Langlo CS, et al. In vivo imaging of human cone photoreceptor inner segments. *Invest Ophthalmol Vis Sci*. 2014;55:4244−4251.
24. Rossi EA, Granger CE, Sharma R, et al. Imaging individual neurons in the retinal ganglion cell layer of the living eye. *Proc Natl Acad Sci U S A*. 2017;114:586−591.
25. Sredar N, Razeen M, Kowalski B, et al. Comparison of confocal and non-confocal split-detection cone photoreceptor imaging. *Biomed Opt Express*. 2021;12:737−755.
26. Guevara-Torres A, Williams DR, Schallek JB. Origin of cell contrast in offset aperture adaptive optics ophthalmoscopy. *Opt Lett*. 2020;45:840−843.
27. Mecê P, Gofas-Salas E, Rui Y, et al. Spatial-frequency-based image reconstruction to improve image contrast in multi-offset adaptive optics ophthalmoscopy. *Opt Lett*. 2021;46:1085−1088.
28. Mozaffari S, Jaedicke V, LaRocca F, et al. Versatile multi-detector scheme for adaptive optics scanning laser ophthalmoscopy. *Biomed Opt Express*. 2018;9:5477−5488.

29. Choi S, Hill D, Guo L, et al. Automated characterisation of microglia in ageing mice using image processing and supervised machine learning algorithms. *Sci Rep*. 2022;12:1806. https://doi.org/10.1038/s41598-022-05815-6.
30. Reddaway J, Richardson PE, Bevan RJ, et al. Microglial morphometric analysis: so many options, so little consistency. *Front Neuroinform*. 2023;17:1211188. https://doi.org/10.3389/fninf.2023.1211188.
31. Guillonneau X, Eandi CM, Paques M, et al. On phagocytes and macular degeneration. *Prog Retin Eye Res*. 2017;61:98−128.
32. Castanos MV, Zhou DB, Linderman RE, et al. Imaging of macrophge-like cells in living human retina using clinical OCT. *Invest Ophthalmol Vis Sci*. 2020;61:48. https://doi.org/10.1167/iovs.61.6.48.
33. Provis JM, Penfold PL, Edwards AJ, van Driel D. Human retinal microglia: expression of immune markers and relationship to the Glia limitans. *Glia*. 1995;14:243−256.
34. Rathnasamy G, Foulds WS, Ling EA, Kaur C. Retinal microglia − a key player in healthy and diseased retina. *Prog Neurobiol*. 2019;173:18−40.
35. Penfold PL, Madigan MC, Provis JM. Antibodies to human leucocyte antigens indicate subpopulations of microglia in human retina. *Vis Neurosci*. 1991;7:383−388.
36. Radolf JD. Treponema. In: Baron S, ed. *Medical Microbiology*. 4th ed. University of Texas Medical Branch at Galveston; 1996.
37. Peeling RW, Mabey D, Kamb ML, et al. *Syphilis. Nat Rev Dis Primers*. 2017;3:1−21.
38. Joseph A, Power D, Schallek J. Imaging the dynamics of individual processes of microglia in the living retina in vivo. *Biomed Opt Express*. 2021;12:6157−6183.
39. Zawadzki RJ, Zhang P, Zam A, et al. Adaptive-optics SLO imaging combined with widefield OCT and SLO enables precise 3D localization of fluorescent cells in the mouse retina. *Biomed Opt Express*. 2015;6:2191−2210.
40. Joseph A, Chu CJ, Feng G, et al. Label-free imaging of immune cell dynamics in the living retina using adaptive optics. *eLife*. 2020;9:e60547. https://doi.org/10.7554/eLife.60547.
41. Gupta V, Al-Dhibi HA, Arevalo JF. Retinal imaging in uveitis. *Saudi J Ophthalmol*. 2014;28:95−103.
42. Muñoz-Fernández S, Uveitis Martín-Mola E. *Best Pract Res Clin Rheumatol*. 2006;20:487−505.
43. Biggee K, Gale MJ, Smith TB, et al. Parafoveal cone abnormalities and recovery on adaptive optics in posterior uveitis. *Am J Ophthalmol Case Rep*. 2016;1:16−22.
44. Errera MH, Coisy S, Fardeau C, et al. Retinal vasculitis Imaging by adaptive optics. *Ophthalmology*. 2014;121:1311−1312.e2.
45. Errera M-H, Laguarrigue M, Rossant F, et al. High-resolution imaging of retinal vasculitis by flood illumination adaptive optics ophthalmoscopy: a follow-up study. *Ocul Immunol Inflamm*. 2020;28:1171−1180.
46. Wang J, Chen S, Zhang X, et al. Intravitreal triamcinolone acetonide, retinal microglia and retinal ganglion cell apoptosis in the optic nerve crush model. *Acta Ophthalmol*. 2016;94:e305−e311.
47. Venkat AG, Sharma S. Automated measurement of leakage on wide-field angiography in the assessment of retinal vasculitis. *J Ophthal Inflam Infect*. 2020;10:4. https://doi.org/10.1186/s12348-019-0193-8.
48. Siddique SS, Suelves AM, Baheti U, Foster CS. Glaucoma and uveitis. *Surv Ophthalmol*. 2013;58:1−10.